Location Estimators for Interferometric Fringes
Author(s): M. Gai, S. Casertano, D. Carollo, and M. G. Lattanzi
Source: *Publications of the Astronomical Society of the Pacific*, Vol. 110, No. 749 (July 1998), pp. 848-862
Published by: The University of Chicago Press on behalf of the Astronomical Society of the Pacific
Stable URL: http://www.jstor.org/stable/10.1086/316202
Accessed: 06/05/2013 21:32

PUBLICATIONS OF THE ASTRONOMICAL SOCIETY OF THE PACIFIC, **110**:848–862, 1998 July

Location Estimators for Interferometric Fringes

M. GAI

Astronomical Observatory of Torino, Strada Osservatorio, 20, I-10025 Pino T.se (TO), Italy; gai@to.astro.it

S. CASERTANO

Space Telescope Science Institute, 3700 San Martin Drive, Baltimore, MD 21218; and The Johns Hopkins University; stefano@stsci.edu

AND

D. CAROLLO AND M. G. LATTANZI

Astronomical Observatory of Torino, Strada Osservatorio, 20, I-10025 Pino T.se (TO), Italy; carollo@to.astro.it, lattanzi@to.astro.it

Received 1997 December 10; accepted 1998 April 15

ABSTRACT. Future global astrometry missions have targeted the determination of positions, parallaxes, and annual proper motions to the 10 μas level. This can be achieved through the use of fringe imaging interferometers, possibly featuring wide fields of view (e.g., Fizeau configurations). The basic location information is to be extracted from the fringe pattern by proper implementation of the detection system and proper exploitation of the focal plane data. The sampling resolution requirements are a key trade-off issue between science and engineering: therefore, fringe acquisition by means of realistic detectors and the resulting accuracy in photocenter location is discussed herein. The location performance is described as a χ^2 minimization problem; the resulting expressions are then evaluated in analytical form and by means of a Monte Carlo simulation, whch provide good agreement. In order to achieve the limiting interferometer accuracy, 8–10 pixels per fringe period are required, whereas a sampling resolution of 4–5 pixels per period provides a 30% degradation. We evaluate the location accuracy degradation induced by progressively reduced fringe visibility and increasing noise level. The former provides a smooth performance reduction, acceptable to a wide extent; read-out noise is critical because the fringe pattern signal is recorded over many pixels, each providing a comparable contribution to the overall noise.

1. INTRODUCTION

The Horizon 2000 Plus Plan of the European Space Agency (ESA) includes a Cornerstone class mission devoted to interferometry. A Survey Committee appointed by ESA reported that one strong recommendation from the scientific community was in favor of devoting such an interferometric cornerstone to global astrometry at the 10 μas level, building on the results of the *Hipparcos* mission (Lindegren & Perryman 1996 and references therein). The Global Astrometric Interferometer for Astrophysics (GAIA) mission concept is now being investigted by the Agency, at the system level, as a candidate for such an interferometric mission.

GAIA will provide positions, proper motions, and parallaxes of $\sim 5 \times 10^7$ stars to a limiting magnitude $V \sim 15$, and possibly fainter, with an accuracy better than 10 μas, along with multicolor, multiepoch photometry for each object, with unprecedented results concerning several fields of astrophysics and cosmology (Lindegren & Perryman 1996). The instrument concept is based on three coplanar interferometers, pointed in directions separated by large *base angles* and operating in scanning mode; this strategy has been derived from the GAIA predecessor *Hipparcos*. The proposed launcher is an Ariane V vector, imposing an envelope ~4 m.

The angular resolution provided by the GAIA interferometer is proportional to its baseline ($B \sim 2.5$ m), but the optical elements involved are smaller, with sizes corresponding to the aperture (diameter $D \sim 0.6$ m); a Fizeau configuration has been adopted as the starting point because of the need for a large field of view (FOV) in order to achieve a reasonable exposure time over each target and superposition between subsequent scans. The baseline optical configuration analysis is available in the literature (Loiseau & Shaklan 1995).

Scanning operations are suitable to a survey instrument, aimed at performing global astrometry with uniform sky coverage. GAIA spins around an axis orthogonal to the plane of the interferometers, and therefore the images move in the focal plane along the high-resolution (scan) direction. The spin rate, precession rate, and field of view are constrained by the mission requirements on sky coverage, multiple observations per target, and measurement accuracy; an acceptable compromise has a precession rate of ~6.4 revolutions yr^{-1}, providing about eight measurements yr^{-1} for each target, a spin rate of ~120 s^{-1}, for a rotation period of 3 hr, and a field of view of ~1° both along

and across the scan direction. The total exposure time per passage will then be ~24 s, which can be broken into 120 elementary exposures of 0.2 s each (see § 2 for the trade-offs on the length of individual exposures).

The focal plane images produced by an interferometer are interference patterns, i.e., fringes, which modulate the overall light distribution— described by the Airy disks corresponding to each aperture— with a period corresponding to the Young period associated with the interferometer baseline. In the case of GAIA, at an operating wavelength $\lambda_{\rm eff} \simeq 550$ nm, the principal Airy disk diameter is $2.44\lambda_{\rm eff}/D \simeq 0\farcs5$, whereas the fringe period is $\lambda_{\rm eff}/B \simeq 46$ mas, which provides a resolution increase of an order of magnitude. The proposed bandwidth is rather large, $\Delta\lambda \simeq 100$ nm, which therefore provides a reduced visibility with respect to the monochromatic case: at increasing distance from the central peak, maxima and minima at different wavelengths are displaced by an increasing amount, so that the overall modulation is degraded. Moreover, for a large-field interferometer, aberrations must be taken into account, as well as finite bandwidth effects, because wave front errors result in a coherence degradation. Actually, the coherent field of view is defined as the region featuring a sufficiently good fringe contrast, e.g., visibility above 70%–80%; optical configuration optimization with the aim of achieving such a high modulation over a ~1° FOV, with a reasonably large bandwidth, has proved to require significant efforts: some comments are reported in § 2, and references therein. From radio astronomy, the modulation of the whole telescope diffraction spot is achieved when $\Delta\lambda/\lambda < D/B$, which is verified in our case; however, even a larger bandwidth will provide some modulation, although limited to the central region of the Airy disk.

The mathematical approach of § 3 is independent of any assumption concerning the amount of modulation, although the system performance *is* sensitive to the fringe contrast: in general, reduced visibility results in progressive accuracy degradation. Therefore, throughout this paper, monochromatic fringes with 100% modulation are usually considered; the fringe visibility is taken explicitly into account in § 6 as an independent parameter, and no tentative system trade-off is suggested here because this is outside our intended scope.

A Fizeau-type interferometer makes use of a limited part of the collecting area provided by the underlying monolithic telescope but takes advantage of all of its image quality: the coherent field of view is basically provided by the corrected FOV of the latter. As far as the residual aberrations of the underlying telescope are small, the interference of the two beams is constructive, and the Airy disk of the subapertures is modulated by the Young period related to their separation, all over the field, in principle providing an improved resolution because part of the low spatial frequencies is suppressed. The first step in order to achieve a large-field interferometer is therefore to design a large-field conventional telescope and then to remove most of the area of the primary mirror (and, optionally, of subsequent optics as well); in practice, the design can become more compact because of the reduced size of the interferometer optics. A sample four-mirror configuration, described in Gai et al. (1997a), is included in Figure 1. The high-resolution position information present in the relative fringe phase of two interferograms is directly encoded in the focal plane image. This allows for a simpler measurement concept than with a Michelson-type interferometer, for which each source has to be observed separately, and the distance among targets is measured essentially by evaluating the phase change required to switch the maximum visibility condition from one of them to another, by means of delay lines.

Such high-resolution information (implicit in the fringe pattern) must be extracted by a suitable algorithm, which we refer to as the *location process*. In this paper, we present an analysis of simple location estimators and derive the expected performance of a CCD array as a function of the geometric sampling resolution, or pixel size, and other system parameters.

In a dilute interferometer, as suggested for GAIA, consisting of two circular apertures of diameter D, separated by a much larger center-to-center distance B, the limiting location error in the along-scan/high-resolution direction is given by (Lindegren & Perryman 1996)

$$\sigma \geq \frac{\lambda}{2\pi B\ \mathrm{S/N}}, \quad \mathrm{S/N} \leq \sqrt{N}, \tag{1}$$

where λ is the effective wavelength, N is the number of photons, and photon-limited performance is assumed. The results presented herein confirm that equation (1) corresponds to the limiting accuracy *in the case of very high sampling resolution.*

The baseline design assumed the use of a modulating grid (see § 2), despite the advantage of direct fringe detection (imaging), because of the technical difficulties of the latter. However, the mission concept is evolving, and some of the configurations now considered increase the effective focal length from the original 11.5 m value to 40–50 m, which provides a better match to state-of-the-art detector geometry. The present paper considers mainly direct fringe detection, addressing the performance of the location process from a strictly geometrical point of view; we do not address issues of feasibility and manufacturability of the detectors.

Several of the critical issues related to an actual implementation of the GAIA concept, highlighted in the Cambridge 1995 Symposium (Lattanazi 1995), have been included in the industrial study contract 12111/96/NL/FM(SC), funded by ESA/ESTEC, awarded to a team led by Alenia Spazio and including the Osservatorio Astronomico di Torino, the Istituto Metrologico "G. Colonnetti"of the Italian National Research Council, Aerospatiale, and Matra Marconi Aerospace. Some of the current results have been presented in Gai et al. (1997a), and a more detailed optical analysis is included in Lattanzi et al. (1997).

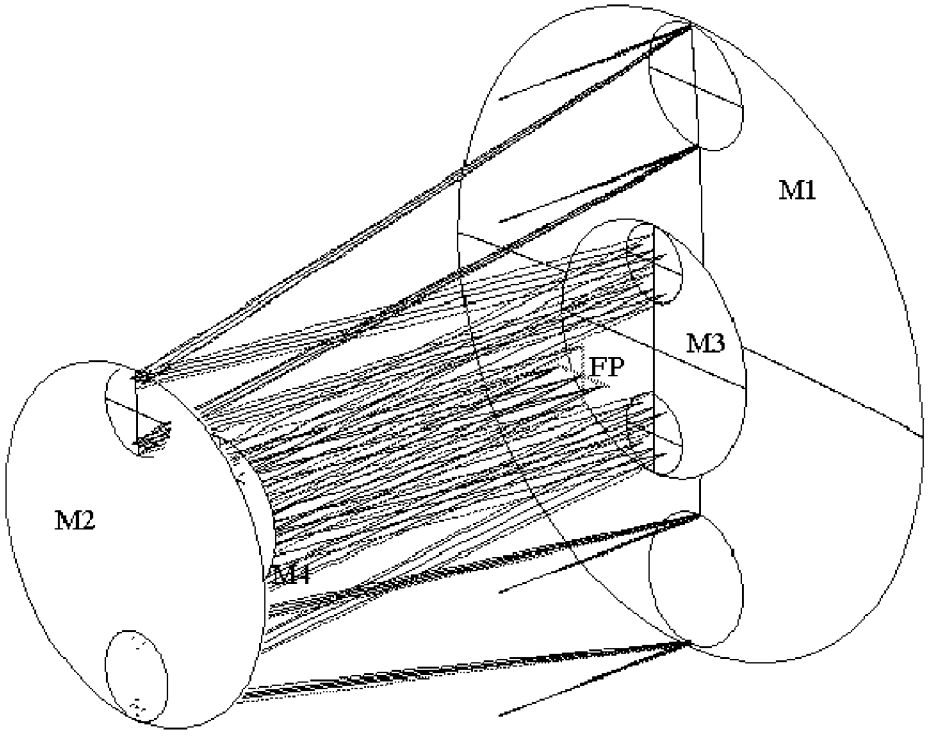

FIG. 1.— Example of large-field interferometer: active regions are cut out of the underlying four-mirror telescope. M1, M2, M3, and M4: primary, secondary, tertiary, and quaternary mirrors; FP: focal plane.

2. DETECTION: MODULATING GRID VERSUS IMAGING

The information on target position is contained in the phase of the interference fringe pattern. The concept of direct fringe detection (or fringe imaging), initially excluded for its technical difficulty although more efficient, requires installing a detector with very high spatial resolution on the focal plane and integrating the fringe images as they move along the field of view; CCDs operated in drift scanning, or time delay integration (TDI) mode, are the most natural choice. TDI is implemented by transferring the potential wells under the CCD electrodes at a clock rate synchronized with the sky motion; for any target, the photocurrent integration lasts for the whole transit onto a single detector, which is read continuously, providing an endless sky strip image (see Gai, Guarnieri, & Lattanzi 1997b and references therein).

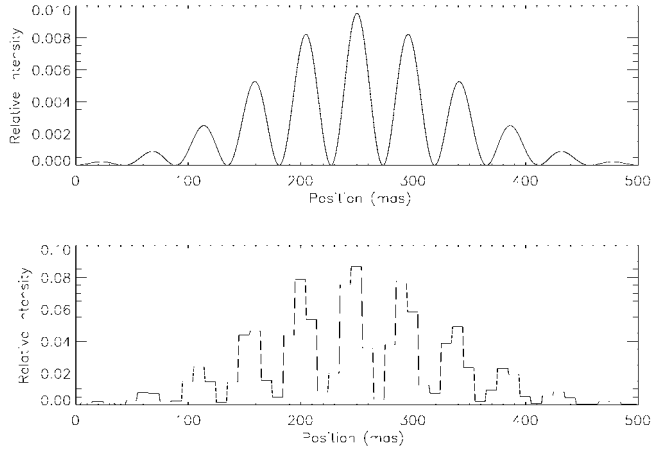

FIG. 2.— Continuous and discretized image profile

This detection scheme was mentioned by the mission proposers in a 1994 technical report to ESA (see Lindegren & Perryman 1996) and was discussed in Gai et al. (1995).

The result of (monodimensional) imaging of an ideal fringe pattern is shown in Figure 2 for a projected pixel size of 10 mas. Even at this rather small pixel size, corresponding to 4.5 pixels per fringe period, the degradation of the image profile is apparent. The rest of this paper is dedicated to quantifying this effect and determining the pixel size and properties required for an acceptable location performance.

With the effective focal length of 12 m advocated in the original design (Loiseau & Shaklan 1995), fringe imaging as good as that shown in Figure 2 would require a pixel size of ~0.6 μm in the scan direction to sample the fringe period over 4 pixels, much smaller than the 5–15 μm pixel size of current

commercial devices. CCD prototypes with pixel size 2.4 μm have been produced and tested (A. Theuwissen, Philips Research Laboratories 1997, private communication) with encouraging results, and some further improvements are possible. Even if improvements in silicon manufacturing technology could achieve submicron-sized CCD pixels, fundamental performance limitations might arise from the reduced well capacity and low quantum efficiency associated with very small pixels and thin devices (thickness must be comparable to pixel size in order to minimize crosstalk among pixels).

The new optical configurations proposed for the GAIA interferometers (Lattanzi et al. 1997 and references therein) achieve the required optical performance with an effective focal length increased to 40 m; with sampling resolution of 3 pixels per fringe period, the required pixel size is ~4 μm, and the resulting focal plane assembly size is ~0.95 m for a ~1° FOV. A further increase in focal length is possible, although difficult, from the standpoint of optical design, but the allocation of a much larger focal plane assembly on the satellite appears impractical.

In the case of direct detection of the fringes, the combination of high spatial and temporal resolution (the latter related to the rapid motion of the images) potentially results in a very high data rate. However, using CCDs as integrating detectors, in TDI mode, temporal resolution is traded for exposure time. For comparison, using positional photon-counting devices (e.g., MAMA), the geometrical requirements imposed by sampling considerations are again critical (i.e., resolution of a few microns), but above all the electronics requirements become overwhelming. The large FOV of GAIA provides simultaneous observation of 10^3 targets simultaneously, on average, and, even assuming the limiting magnitude flux for each (~3×10^3 photons s^{-1} at $V = 15$ mag), at 100% quantum efficiency, this results in a mean throughput of 10^6 events s^{-1} to be detected, time-tagged, and stored or integrated in digital form (short-term variability is not an issue for most of the GAIA targets). Since the resolution required by the across- and along-scan coordinates are, respectively, on the order of 1″ and 10 mas, which calls for 12 and 19 bits resolution over the 1° FOV, the overall data rate would be on the order of 10^8 bits s^{-1}. Such throughput might be considered feasible, although demanding, but this does not take into account that crowded regions are interesting for several astrophysical reasons. Local target density may easily be 1 or 2 orders of magnitude higher than the average values noted above, which would therefore provide extremely stringent electronics requirements, or a saturation problem (at the detector level and/or in the readout circuitry), which would directly impact the mission's scientific yield.

Moreover, the quantum efficiency of good photon-counting detectors is at best a few percent, owing to photocathode material, to be compared with values of 10%–20% for comparably poor CCDs and up to 80%–90% in the most favorable cases. This might slightly alleviate the data rate problem, at the expense of a dramatic degradation of the instrument performance. Although development is nonetheless required, in order to optimize them for GAIA, CCDs appear to be the detectors of choice in the near future.

The alternative detection strategy to direct fringe imaging relies on modulating grids, consisting, for example, of a series of slits in front of a small region of the focal plane, with the nominal fringe period. Each grid, during the transit of a target over the corresponding sky region, modulates the interference pattern and thus produces a time-dependent signal that can be recorded by the detector with much lower spatial resolution than that required for imaging. The modulating grid intrinsically degrades the high-frequency information of the fringe pattern and, in its simplest implementation, causes ~50% of the photons to be lost (reflection or opacity of the grid). Direct fringe detection provides better astrometric performance, with a gain ideally between a factor 2 and 4, and fainter limiting magnitude.

An important design parameter for both direct fringe detection and modulating grid is the size of the elemental observation, corresponding to traversing a single detector or grid element, respectively. A longer elementary observation provides better S/N and a fainter limiting magnitude, at the expense of increasing the degradation of the fringe contrast owing to possible pointing and spin jitter and to field-dependent optical distortions. In addition, the elemental integration in the case of the modulating grid is limited by the problem of confusion ("spoilers"), as all sources within the grid area will contribute to the total measured signal in a time-dependent way, with a consequent distortion of the measured position. A grid size of 27″ was chosen in the baseline design, which corresponds to a transit time (and thus exposure time) of 0.225 s, probably an upper limit for the grid design. We generally assume a similar elementary exposure of 0.2 s for direct fringe detection, but we are currently exploring a number of design aspects of the interferometers and of the satellite that could allow for longer exposure times.

A significant astrometric performance improvement toward the grid option might therefore be provided even by a suboptimal fringe imaging system.

The scenario analyzed in the rest of this paper assumes direct imaging of the fringe system. Since GAIA performs accurate measures only in the direction of the fringe system, i.e., along the scan direction, we will discuss primarily position measurements in that direction. The two-dimensional position is reconstructed a posteriori from several one-dimensional positions obtained form different scans, each with a different orientation on the plane of the sky. For convenience, we will assume that the pixel size in the across-scan direction is larger than the diameter of the Airy disk; in this case, the fringe pattern is actually integrated in the low-resolution direction, and the image profile as seen by the detection system is basically unidimensional. This approach simplifies both the engineering problems (e.g., the telemetry data rate) and the data processing framework. However, our conclusions apply equally well to a

fringe pattern integrated across the scan direction *after* the observation, to each slice of a well-sampled interferogram or, with appropriate minimal changes, to the bidimensional problem.

3. LOCATION PROCESS

The image *location process* is an algorithm aimed at extracting the target position information, i.e., the photocenter, considered to be the "true position" of the image. The astrometric interest in this problem is to find target locations in the sky with the highest possible accuracy: the advantage of an interferometer, with respect to a single filled aperture of equivalent collecting area, is the increased resolution in one dimension thanks to the high spatial frequency information in the interference fringes.

The first step toward determining the astrometric coordinates is the measurement of the position of a signal packet (for GAIA, the set of interference fringes) with respect to a focal plane reference system, such as that defined by a detector made of an array of pixels. Hereafter, only the one-dimensional case will be considered, as relevant for GAIA, although most of our considerations will readily extend to two or more dimensions. The position of the signal packet is defined with respect to a reference point in the packet itself, such as its geometric center if the packet is mirror-symmetric; we will use the generic expression "photocenter" for this reference point. We assume that the system response is perfectly known and translationally invariant; we can then introduce a function $f(x)$ such that the system response to a packet placed at a "true" position τ_0 will be $f(x - \tau_0)$.

The function $f(x)$ is akin to a point-spread function, in that it describes the system response to a stimulus placed in the origin; for an idealized GAIA interferometer, $f(x)$ describes the fringe packet corresponding to an on-axis point source [then in fact $f(x)$ *is* the PSF of the system]. The target placed at τ_0 will be described by $f(x - \tau_0)$, scaled by the appropriate intensity.

This problem has been considered in detail by Lindegren (1978), who addressed primarily the idealized case in which $f(x - \tau_0)$ can be measured with arbitrary resolution, albeit with finite noise. Instead, we consider specifically the case of a discrete sampling of the signal, for example by an array of finite-sized pixels.

The measurement problem is defined by a least-squares approach; this differs somewhat from Lindegren's treatment, which is based on finding the zero(s) of a functional $g(x)$, defined by convolving the observed signal with an appropriate weight function (see eq. [13]). Lindegren's approach is a generalization of the conventional center of gravity definition. While the two approaches are to a large extent equivalent, the least-squares formulation provides a convenient conceptual framework; Lindegren's results can be recovered from our treatment, with only minor modifications that will be pointed out explicitly hereafter.

Apart from the noise contributions, the detected signal can be expressed in terms of the pixel response function $h(x)$, which we assume to be the same for all pixels. From the PSF $f(x)$, the signal S_n from a pixel centered at x_n is

$$S_n = \int_{-\infty}^{+\infty} f(x)h(x - x_n)dx. \tag{2}$$

For an "ideal" pixel of width Δ, the response will be constant between $(x_n - \Delta/2)$ and $(x_n + \Delta/2)$ and zero outside, so $h(x)$ is, apart from a normalization constant,

$$h(x) = 0(x < -\Delta/2)$$
$$h(x) = 1(-\Delta/2 < x < \Delta/2)$$
$$h(x) = 0(x > \Delta/2).$$

The (noiseless) signal detected in an ideal pixel centered at x_n is

$$S_n = \frac{1}{\Delta}\int_{x_n-\Delta/2}^{x_n+\Delta/2} f(x)dx,$$

where the normalization is such that in the continuum limit $(\Delta \to 0)$, the discretized signal S_n reduces to the parent distribution $f(x)$.

In order to discuss the case of discrete pixels, either ideal or real, we define the (continuous) pixel response function $\tilde{f}$ as

$$\tilde{f}(x) = \int_{-\infty}^{+\infty} f(y)\ h(y - x)\ dy, \tag{3}$$

which can be considered as the *effective* PSF, taking into account the finite pixel size; the pixel signal from equation (2), generated by a packet centered in the origin, in a pixel centered at x_n, is therefore $S_n = \tilde{f}(x_n)$, whereas in the case of a fringe pattern centered at τ_0,

$$S_n = \tilde{f}(x_n; \tau_0) = \int_{-\infty}^{+\infty} f(y - \tau_0)h(y - x)\ dy. \tag{4}$$

Each measurements is affected by an error e_n, which is assumed to be *unbiased* and *uncorrelated* among pixels:

$$\langle e_n \rangle = 0\langle e_m e_n \rangle = \sigma_n^2 \delta_{mn}. \tag{5}$$

The actual measured signal for pixel n, and the associated variance, taking into account as error sources only the CCD read-out noise (hereafter RON) R and the photon shot noise,

are

$$s_n = S_n + e_n \text{ and } \sigma_n^2 = R^2 + S_n. \tag{6}$$

Its continuous analog $s(x)$ can be defined similarly, except that care must be exercised to define the sampling scale for the noise terms.

3.1. Least-Squares Estimation

A measure (τ) of the "true" position (τ_0) can be obtained by least-squares fitting of the measured signal s_n with the model provided by $\tilde{f}$, using the classic definition of χ^2:

$$\chi^2 = \sum_n \frac{[s_n - \tilde{f}(x_n; \tau)]^2}{\sigma_n^2}. \tag{7}$$

The values of τ corresponding to a stationary point of χ^2 are the solutions of the equation

$$\sum_n \frac{[s_n - \tilde{f}(x_n; \tau)]\,\tilde{f}'(x_n; \tau)}{\sigma_n^2} = 0, \tag{8}$$

where the prime indicates derivative with respect to the first argument, and we have used the fact that $\partial\tilde{f}(x; \tau)/\partial\tau = -\tilde{f}'(x; \tau)$.

From equations (4) and (6), in case of small errors, the term in square brackets is small for $\tau \approx \tau_0$. Here, expanding $\tilde{f}$ in Taylor series and retaining only the leading order in $\tau - \tau_0$:

$$\sum_n \frac{[e_n + \tilde{f}'(x_n; \tau)(\tau - \tau_0)]\,\tilde{f}'(x_n; \tau)}{\sigma_n^2} \approx 0 \tag{9}$$

$$\tau - \tau_0 = -\frac{\sum_n e_n \tilde{f}'(x_n; \tau)/\sigma_n^2}{\sum_n [\tilde{f}'(x_n; \tau)]^2/\sigma_n^2}. \tag{10}$$

Using equation (5), the estimate of τ_0 (which results unbiased) and its variance are

$$\langle(\tau - \tau_0)\rangle = 0$$

$$\langle(\tau - \tau_0)^2\rangle = \frac{1}{\sum_n [\tilde{f}'(x_n; \tau)]^2/\sigma_n^2}. \tag{11}$$

Two additional points are worth noting. First, the formulæ above are based on the assumption that higher order terms in the Taylor expansion can be neglected. This is not necessarily the case if the expected error is significant compared with the typical scale of f, which, for interference fringes, means that the positioning error must be small compared with their half-period. Explicitly, the treatment above is valid only if

$$\langle(\tau - \tau_0)^2\rangle^{1/2} \ll \lambda_Y/(2\pi), \tag{12}$$

where λ_Y is the characteristic length of the signal packet ($\lambda_Y \sim 2\pi|\tilde{f}/\tilde{f}''|^{1/2}$). If this condition is not satisfied, which can happen if the signal-to-noise ratio is poor, then the "optimal" estimator (in the χ^2 sense) given by equation (8) may well be less desirable than other, more robust estimators.

Second, equation (8) can have multiple solutions, corresponding to different stationary points of the χ^2 value; this is routinely the case when the function $\tilde{f}$ has multiple peaks (again, as in the case of interference fringes). In this case, the value of the χ^2 itself can be used to identify the "true" minimum. For practical purposes, a first approximation can be provided, e.g., by an input catalog or by a simple center-of-gravity algorithm.

3.2. Connection with Lindegren's Estimators

As remarked earlier, our treatment is closely related to that given in Lindegren (1978), who defines the "location estimator" as the zero of an appropriate functional $g(\tau)$ formed as the scalar product of the signal with a weight function $w(x)$:

$$g(\tau) \equiv \int s(x)w(x - \tau)dx = 0. \tag{13}$$

Different choices of the weight function correspond to different location estimators. Lindegren's discussion focuses mainly on the continuum case; the discrete case receives only a cursory mention, and some of his assumptions are not optimally suited to the discrete case.

It can easily be shown that, in the case of a continuum detector (with the pixel response function replaced by a Dirac delta), for Poisson and white noise, respectively, the approach outlined above provides Lindegren's optimal weighting functions given in his equations (10) and (13). Similarly, we straightforwardly reproduce the results of his §§ 5.3 and 5.4, for a continuum detector.

On the other hand, Lindegren's equation (3b) for the discrete case is equivalent to our equation (8), with two important provisions:

1. $\tilde{f}$, the signal integrated in a pixel, should replace f in Lindegren's equation (1b) and wherever f appears.
2. The functional definition (eq. [13]) needs to be modified according to equation (8), which provides the new definition for $g(\tau)$:

$$g(\tau) \equiv \sum_n [s_n - \tilde{f}(t_n; \tau)]\,w(t_n; \tau) = 0. \tag{14}$$

The additional term in square brackets in equation (14) is required in order to satisfy the condition for unbiasedness expressed in Lindegren's equation (5), modified for the discrete case. Without this change, the $g(\tau)$ estimator would be unbiased only for those special combinations of PSF, pixel response, and weight function for which

$$\sum_n \tilde{f}(t_n; \tau) w(t_n; \tau) \equiv 0.$$

Somewhat coincidentally, this condition is satisfied, for ideal pixels, by the optimal weight for pure Poisson noise, which is

$$w_{\rm P}(x) = \tilde{f}'(x)/\tilde{f}(x). \tag{15}$$

By comparing equations (8) and (14), we find that the Lindegren's functional equivalent to our least-squares approach is defined by the weighting function

$$w(x) = \frac{\tilde{f}'(x)}{\sigma^2}. \tag{16}$$

For a generic weighting function $w(x)$, the variance of the location estimate can be deduced under appropriate conditions as

$$\langle (\tau - \tau_0)^2 \rangle = \frac{\sum_n \sigma_n^2 w^2(x_n; \tau)}{\left[\sum_n \tilde{f}'(x_n; \tau) w(x_n; \tau)\right]^2}. \tag{17}$$

Some of the advantages of Lindegren's definition of the location estimator as the zero of the functional $g(\tau)$, for both the continuum and discrete cases, are its simplicity, generality, and flexibility. By changing the weight function $w(x)$, this estimator allows for a consistent treatment of a number of different problems under the same formalism, including, as special cases, most useful location estimators, such as the least-squares estimate. It also includes explicitly some nonoptimal, but robust, location estimators, such as the mean and the median. These can also be accommodated in the least-squares approach by fitting the signal with an appropriate function (for example, the triangle for the median), but this solution is formally less elegant.

On the other hand, the approach of casting the method explicitly as a weighted least-squares optimization also has some useful properties. First, it is easier to find the optimal weights for an arbitrary noise model, and the resulting estimator is guaranteed to be optimal in the least-squares sense. Second, the method generalizes easily to the case of low signal-to-noise ratio, and it does not require that the differences between estimated and true position be "small," although our conclusions on the expected variance of the result do depend on that assumption. Third, having the method expressed explicitly as a variational principle allows us to deal properly with multiple solutions [multiple zeros of $g(\tau)$] by choosing the stationary point with the smallest value of χ^2.

4. PREDICTED PERFORMANCE

We now progress to apply equations (11) and (17) to estimate analytically the location error as a function of pixel size for several weighting functions. We consider specifically the case of a source producing 2000 photoelectrons, which would be appropriate to the GAIA baseline design for a $V = 12.5$ mag star in an elementary integration of 0.2 s. The assumed bandwidth ($\Delta\lambda \simeq 100$ nm) and operating wavelength ($\lambda_{\rm eff} = 550$ nm) actually cause some marginal visibility degradation, which is neglected throughout the initial analysis; the sensitivity of our results to changes in visibility over a substantial range is discussed in § 6. We consider Poisson noise only, as in this regime the sky background and the detector noise are likely to be negligible. The "ideal" measurement accuracy predicted by equation (1) in this case is 165 μas.

A similar performance could be achieved for a fainter target if a longer individual exposure time proved possible. In the regime in which Poisson noise from the target signal dominates, the performance scales so that a target 1 mag fainter would require an exposure time of 0.5 s to achieve the same elemental performance.

In order to investigate a variety of options, we consider three location estimators described, in the Lindegren approach, by different weighting functions. The first is the optimal weighting function in the case of pure Poisson noise only, $w_{\rm P}(x)$ (eq. [15]). The second is the weight function corresponding to a cross-correlation approach, $w_c(x) = \tilde{f}'(x)$, which is optimal when read noise dominates. The third is an ad hoc weight $w_s(x)$ consisting of a sine function with period equal to the Young period of 46 mas. The first two cases can be described in our formalism by the corresponding weights (Poisson noise weight for $w_{\rm P}$, and equal weights for w_c), while the third does not have an immediate analog in our formalism and is included in order to show the effect of a lack of detailed knowledge of the PSF of the system— the sine is a "generic" periodic function and could be used in the absence of a system-specific PSF model.

The results, over a resolution range corresponding to pixel sizes from 1 to 21 mas, are shown in Figure 3. We recall that the limiting pixel size, from the Nyquist-Shannon sampling criterion, is below 23 mas.

The asymptotic value (for arbitrarily small pixels) for $w_{\rm P}$ is ~165 μas, consistent with equation (1). As expected, the other weight functions do not perform as well and have asymptotic values of ~235 and ~250 μas for w_s and w_c, respectively.

The behavior of the error for small pixels can be described approximately by a quadratic function of the pixel size Δ, in

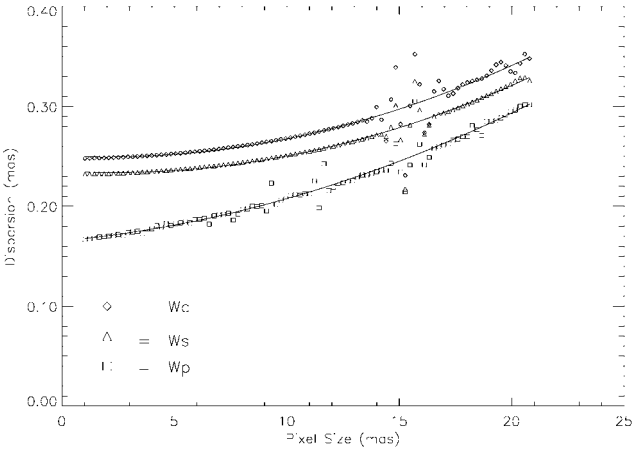

FIG. 3.— Estimated dispersion vs. pixel size

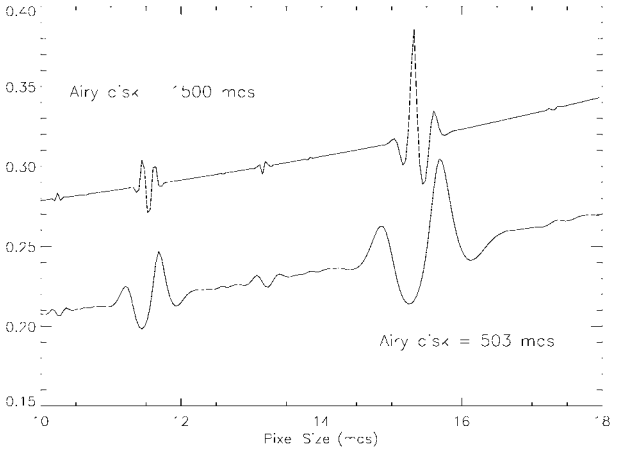

FIG. 4.— Estimated dispersion vs. pixel size for different PSF envelopes. The larger Airy disk case is displaced vertically by 0.07 mas for graphical clarity.

mas, as follows:

$$\sigma_P = 0.1655 + 2.06 \times 10^{-3}\,\Delta + 2.16 \times 10^{-4}\,\Delta^2 \quad (18)$$

$$\sigma_s = 0.2340 - 9.08 \times 10^{-4}\,\Delta + 2.61 \times 10^{-4}\,\Delta^2 \quad (19)$$

$$\sigma_c = 0.2493 - 7.24 \times 10^{-4}\,\Delta + 2.62 \times 10^{-4}\,\Delta^2. \quad (20)$$

The difference among the three curves becomes smaller and smaller for increasing pixel size, which corresponds to increasing discretization noise, but the relative quality of the estimators is preserved: $\sigma_P < \sigma_s < \sigma_c$, i.e., the optimal performance of w_P is confirmed, whereas the sinusoidal function w_s provides intermediate results between w_P and the correlation technique.

As could have been expected, the performance of the three algorithms degrades substantially as the sampling approaches the Nyquist-Shannon limit of two samples per fringe (corresponding to pixel size ~23 mas). Moreover, it should be noted that the dispersion profiles are affected by a sharp oscillation for pixel size ~15.5 mas, corresponding to one-third of the Young period, and that σ_P features at least two other small fluctuations corresponding to higher harmonics: 11.5 mas and 9 mas, i.e., one-fourth and one-fifth of the period. These latter features are not apparent in the profiles provided by the two other weighting functions, w_s and w_c. Perhaps the fluctuations are less noticeable because the intrinsic dispersion of the other algorithms is comparatively larger, but it is also possible that the other algorithms are more robust and thus less affected by these fluctuations.

The actual behavior of each location process, in particular in the critical regions, has been investigated in more detail in the Monte Carlo simulations; hereafter, the comparison with the result of a configuration variation is discussed, whereas the actual simulation results are presented in § 5.3.

The conditions of the sampling theorem are not verified, since the signal is not strictly periodic, because of its finite length; therefore, some reconstruction problem might be expected. In order to assess this issue, the estimated performance has been evaluated for a different configuration, with a PSF envelope ("Airy disk") of about 1500 mas against the original 503 mas; this roughly corresponds to reducing the interferometer apertures, but since the number of photons has not been scaled for any factor, the estimated astrometric performance is referred to brighter targets. In this case, the same sampling resolution is evaluated, but a larger number of significant samples is collected.

The results are shown in Figure 4: the underlying limiting curve, shown here with a vertical displacement of 0.07 mas for clarity, is basically unchanged. The same irregularities are present, corresponding to simple ratios between the fringe and pixel periods; however, the perturbed region extension is reduced. In other words, increasing the length of the signal packet reduces the "resonant" behavior. However, the issue of critical resolution regions might be evaluated in more detail, from a mathematical standpoint, in future work.

The issue of location consistency for such sampling resolution regions has been tested in more detail in our simulations, and the results (shown in Fig. 6) will be discussed in § 5.3.

5. THE MONTE CARLO SIMULATIONS

In order to assess the performance and the implementation peculiarities of the location processes described, a set of simulations has been carried out, which act separately on each of the several parameters involved.

The first test is suggested by the results on potentially critical sampling resolution regions presented in the previous section. In this test we vary the shape of the overall PSF envelope, corresponding to the single-aperture Airy disk, and evaluate its impact on the algorithm performance.

The second test compares the results of the various estimators

with the analytic predictions presented in the previous section, assuming photon-noise–limited performance over a sampling scale from 1 to 21 mas (46–2.2 samples per fringe period). We consider specifically the case of 2000 photoelectrons per sample, corresponding to a 0.2 s TDI exposure of a relatively bright target ($V = 12.5$). We evaluate the algorithmic performance in terms of accuracy and consistency of the results, as well as of processing requirements.

Next, we evaluate the effect of degraded visibility and the contribution of other noise sources, such as read-out noise. The latter is relevant to extend our results to fainter magnitudes, where detector noise may be important. However, a full discussion of the actual "limiting magnitude" for these estimators depends on several other parameters, such as elementary exposure time, operating wavelength, and optical configuration, and therefore is beyond the scope of this document.

Concerning the overall processing structure, a first-order location estimate is provided by the signal center of gravity, used also as a consistency check. At the signal level mentioned, the typical center-of-gravity dispersion is 1–2 mas, mostly independent of pixel size, visibility, and read-out noise, much larger than the values provided by the estimators of interest.

For a given pixel size and a priori photocenter position τ_0, we first compute the discretized image profile $\tilde{f}(x; \tau_0)$ at each pixel position ($x = x_n$) and then generate a set of 10,000 samples, each with a different realization of the Poisson noise. The nominal ("true") position τ_0 of the fringe packet can be placed at some offset with respect to the origin of the coordinates in order to include the effects of varying the relative phase between the pixel array and the signal.

For each specimen, three location algorithms are applied, namely the maximum correlation technique (w_c), the sinusoidal weighting function (w_s), and the optimal weight for Poissonian noise only (w_P). These different weighting functions have been used in order to evaluate their relative performance, robustness, and computational load. Each uses an interpolation mechanism in the neighborhood of the first-order location estimate, computing the values of the functional (14) in a set of points and finding the root (or maximum, for the case of correlation) of the interpolating function.

Mean and standard deviation of the set of locations provided by each estimator are evaluated in order to assess the consistency and the performance of the location process.

At this stage, we are interested primarily in the performance of the location process, and thus we have not considered the problem of target *detection* and *identification*. Future developments will include a more general, multiple-pass algorithm that includes the detection and identification of possible targets. However, it must be noted that, for on-orbit operations of a GAIA-like mission, additional information may be available to help identify the possible targets, such as an input catalog or the incoherent focal plane data provided by auxiliary instrumentation.

The simulations have been developed and performed in the Interactive Data Language environment (IDL version 4.0.1, from Research Systems, Inc., Boulder, CO), running on a PC-compatible desktop computer, equipped with an Intel Pentium/200 MHz processor and 32 MB RAM.

5.1. Fringe Packet Envelope

The relevance of the actual Airy disk profile has been verified by running tests based either on a Gaussian curve or on a damped sinusoidal curve ($[\sin x/x]^2$). In both cases, a 100% modulation with the Young period (46 mas) has been applied: this corresponds to a nearly monochromatic case, whereas our photon budget is based on a rather large bandwidth (100 nm). As discussed in § 6, small performance degradations are induced by visibility reduction when the original value is reasonably high, and in any case the modulation term is the same for both profile options.

For a given overall geometry of the interferometer, the algorithm performance is not overly sensitive to the detailed form of the PSF, as long as the main image parameters (Airy disk size and fringe period) remain fixed. The limiting location accuracy for the continuous case and the dispersion increase with the pixel size are the same for both profiles, down to the 1% level; eventually, a detailed accuracy assessment must be performed on the actual interferometer PSF, as provided by ray-tracing packages.

Since the exact shape of the PSF appears to be unimportant, most further simulations use a Gaussian image profile, represented by the function

$$f(x) = \left(1 + \cos\frac{2\pi}{T_Y}x\right) \exp\left(-\frac{x^2}{2\sigma^2}\right),$$

where $T_Y = 46$ mas is the Young period, and the Gaussian width is defined by the requirement $3\sigma = T_A/2$, corresponding to a fringe packet basically limited to the main Airy disk ($T_A = 503$ mas).

5.2. Location Dispersion

The center-of-gravity algorithm features low sensitivity to the pixel size, as expected, because it does not exploit the detailed information on the shape of the PSF. The corresponding plot, out of scale with respect to the estimators of interest, is not shown here.

The data dispersion versus pixel size, for the three main estimators, is shown in Figure 5, and the overall trends are in good agreement with the predicted performance.

Fitting the relation between the standard deviation σ and the pixel size Δ (in mas) to a quadratic curve, we have

$$\sigma_P = 0.1669 + 1.69 \times 10^{-3}\,\Delta + 2.34 \times 10^{-4}\,\Delta^2 \quad (21)$$

$$\sigma_s = 0.2367 - 1.44 \times 10^{-3}\,\Delta + 2.86 \times 10^{-4}\,\Delta^2 \quad (22)$$

$$\sigma_c = 0.2484 + 1.49 \times 10^{-6}\,\Delta + 2.13 \times 10^{-4}\,\Delta^2. \quad (23)$$

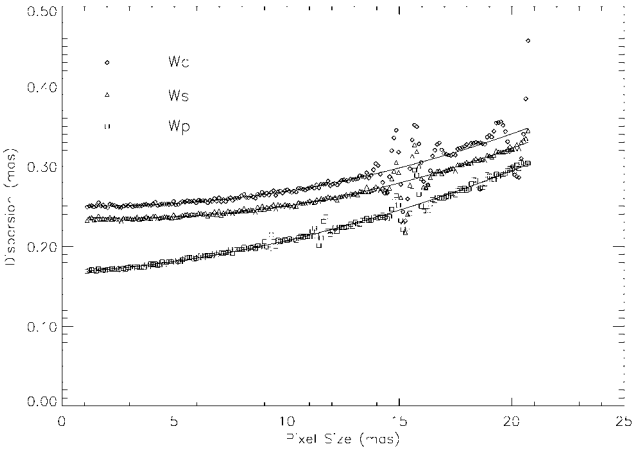

FIG. 5.— Simulated dispersion vs. pixel size

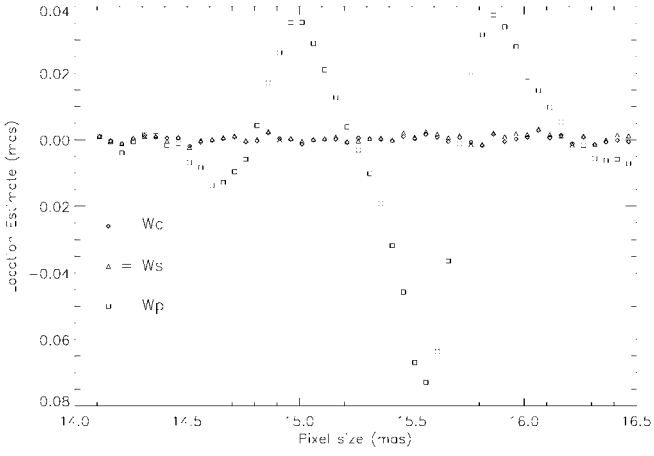

FIG. 6.— Simulated data discrepancy vs. pixel size (region = 14–16.5 mas)

Note that, although the accuracy degrades smoothly with increasing pixel size, even a "good" sampling resolution, such as 4–5 pixels per fringe period, actually causes a significant loss of astrometric performance. For example, at a pixel size of ~10 mas, the photocenter dispersion achieved by the optimal estimator is 0.21 mas, or 27% worse than the "ideal" value of 0.166 mas achieved with very small pixels. For pixel size ~20 mas, the w_p estimator features a location standard deviation of $\simeq$0.3 mas, i.e., 80% larger than the limiting error. The loss of performance between the 10 and 20 mas cases is about 50%; this loss must be carefully weighed against the likely engineering and construction problems associated with a smaller pixel size.

Apart from the individual estimator behavior, two relevant global conclusions can be stated:

1. The performance gap among the three estimators decreases with the sampling resolution, owing to the intrinsic image degradation related to integration over the finite pixel size.
2. Location accuracy within 10% of the "optimal" performance is obtained only with 8–10 pixels per fringe period, corresponding to a pixel size of 4–5 mas.

5.3. Location Consistency

The estimated location value versus pixel size is evaluated over the same 10,000 sample set for each of the estimators.

All three estimators provide a satisfactory consistency over most of the resolution range considered, i.e., 1–21 mas, providing unbiased estimates within the corresponding data dispersion; since the data set is of 10^4 samples, the mean value dispersion is 1/100 of the parent population dispersion (0.2–0.3 mas), i.e., 2–3 μas, and most of the data are within $\pm 3\,\sigma$ from the nominal value. A relevant discrepancy with respect to the overall trend can be found over the critical regions of § 4: whereas the values provided by w_c and w_s are quite consistent between themselves and with the above statistics, since their values are all inside a ± 10 μas range from the a priori value, the w_p estimator provides values affected by a relevant systematic error. The pixel size region affected by such "oscillation," shown in Figure 6, ranges between 14.8 and 16.2 mas, i.e., the critical resolution region close to 3 pixels per fringe period.

A similar behavior can be found in the other critical regions identified by the dispersion estimate.

Since w_p has been derived with the purpose of exploiting as far as possible the detailed shape of the PSF, taking into account the finite pixel size, it seems to be likely that phase dependences might arise. Phase-dependent effects might introduce the systematic effects observed in the simulations because, once the a priori photocenter position is fixed, the pixel size variation modifies the phase of the fringe pattern with respect to the pixel array. This has been checked by running the simulations at fixed pixel size (15.5 mas, corresponding to the most critical region) and varying the fringe pattern a priori position over a range of ± 8 mas, corresponding to more than 1 pixel. For each phase value, a data set of 10^4 samples is generated and processed as described above.

As shown in Figure 7, the discrepancy between the location evaluated by the algorithms and the nominal value confirms the phase-dependent behavior of w_p, whereas the results from w_s and w_c are basically unbiased. Averaging over the phase range, in fact, the mean discrepancy of *each* estimator is quite compatible with zero, but the standard deviation of w_p suffers quite a large increase (~0.24 mas) with respect to the single-phase case statistics. Actually, the results of w_s exhibit some potential residual phase dependence, an order of magnitude smaller than the w_p case, since their linear correlation coefficient is -0.93; the w_c estimates are essentially uncorrelated with the relative phase (correlation coefficient -0.07). However, the interest for w_s is marginal, because it was included as a reference alternative approach (and for a sanity check); a more detailed analysis may be left to future activity.

The dispersion oscillations are still present, as shown in Figure 8, which suggests again a possible phase sensitivity for all

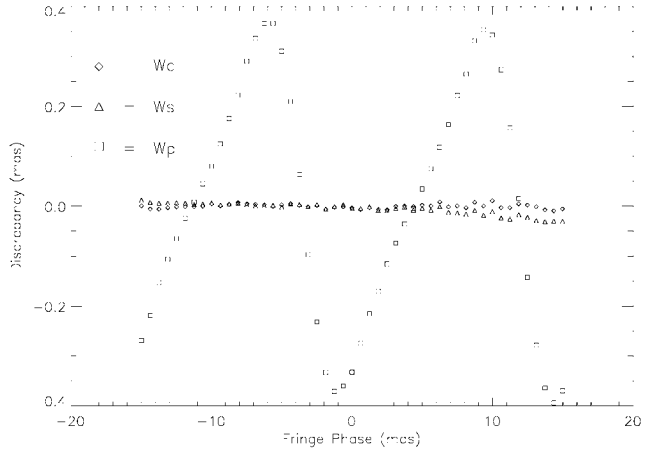

FIG. 7.— Location discrepancy vs. fringe pattern phase (pixel size= 15.5 mas).

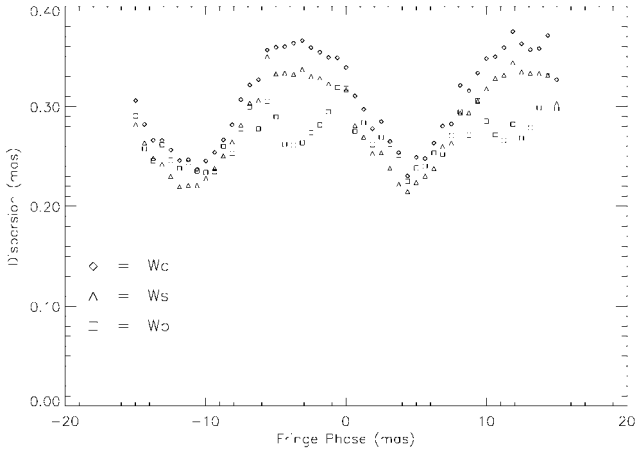

FIG. 8.— Location dispersion vs. fringe pattern phase (pixel size= 15.5 mas).

three estimators; however, the locations provided by w_s and w_c are essentially correct, as discussed above and shown in Figure 7, which confirms that an actual systematic error is introduced only for the w_P case.

It should be emphasized here that Figures 7 and 8 correspond to a worst case scenario, with the pixel size chosen exactly so as to "beat" with the period of the signal. Running the same test for a pixel size chosen in a noncritical region, the location evaluation provides unbiased results (within the statistical errors) for all three estimators. Besides testing other critical regions, the same kind of oscillations arise, although with reduced amplitude, for w_P, whereas the behavior of the other two algorithms is extremely regular and is not affected by the above bias.

Therefore, the optimal estimator w_P, although providing in general the best performance in terms of location dispersion, is not appropriate when the pixel size is in a simple ratio with the fringe period. In a realistic system, the relative advantages of choosing a more sensitive location estimator, optimal in the sense of S/N, must be carefully weighted against any possible systematic errors and biases to which this estimator might lead.

The problem of getting the correct answer from w_P might be practically solved by inserting an ad hoc correcting term, without the benefit of any mathematical support from our previous derivation, e.g., obtained directly from the simulations by a calibration procedure evaluating the discrepancy with respect to the a priori value. However, it would be most appropriate to extend our mathematical description in order also to include in the "effective PSF" the pixel phase effects.

This will be an issue for future improvements.

5.4. Processing Performance

The three algorithms are based on root or maximum finding of a functional, evaluated as a scalar product between the current data set and the weighting functions, tabulated in an appropriate interval; therefore, neglecting the table preparation time, the location estimate has the same computational load for all the above estimators. Of course, the lower resolution cases are processed more rapidly, because a smaller number of pixels is involved. Our procedures are not optimized with respect to the execution time; however, generation and processing of 10^4 simulated data samples requires ~40 s, for pixel size >5 mas. The single data set generation and processing time, using all three algorithms, is therefore ~4 ms.

Processing the whole data set corresponding to the ~1000 targets simultaneously present, on average, in the GAIA field of view, acquired after an exposure of 0.2 s, will require about 4 s, using the three estimators, on a single processor unit comparable to an off-the-shelf desktop PC. On-board data processing would require about 20 times as much computing power, which might be feasible for the GAIA mission.

Although the scientific data reduction, including sphere reconstruction, is in any case likely to be implemented on the ground, the possibility of extracting some intermediate-level informations from the data directly on the satellite might allow monitoring of the optical configuration from the focal plane data. Besides, since several subsequent elementary exposures are obtained from each target during the single transit over the FOV, the possibility of combining immediately, in the best possible way, the subsequent position estimates in order to achieve a single abscissa coordinate for downloading might represent an efficient, lossless data compression scheme, which would therefore alleviate the stringent telemetry requirements. Both issues, although not relevant to the strictly mathematical problem of fringe location, might prove very interesting for the purpose of actual design implementation of the GAIA mission and, in general, for monitoring and control of any large-field interferometer, used either in pointing or in scanning mode.

6. VISIBILITY

Fringe visibility can be defined (in our unidimensional case) as the ratio between the difference and the sum of the maximum and the minimum values of the central interference fringe:

$$V_b = \frac{F_{\max} - F_{\min}}{F_{\max} + F_{\min}}. \tag{24}$$

Visibility is a dimensionless quantity representing the fringe contrast, and in case of reduced visibility a significant loss of information can be expected. Moreover, since the location process is based on specific assumptions on the image profile, in principle any visibility degradation can compromise the performance of the algorithms because of the mismatch between the theoretical and real distributions.

In a real interferometer, owing to finite wavelength bandwidth $\Delta\lambda$, cophasing imperfections, optical aberrations and other effects, fringe contrast is always less than 100%. The visibility can be expected to assume its maximum value at the center of the FOV, for symmetry, and to decrease for increasing distance from the optical axis because of the build-up of aberrations. Also, the finite pixel size contributes to reducing the visibility because of the signal integration over a finite region (see Fig. 2). Visibility is an issue for the initial and periodic set-up and calibration of the instrument: the interferometric configuration must be acquired by tuning the controlled optical components; the maximum visibility value over the whole coherent FOV is a basic requirement. Therefore, at least some of the algorithms must be able to account for degraded visibility, providing consistent results in any case, although with lower accuracy.

A simulation has been run in order to evaluate the effects of degraded visibility on the location algorithms, using the sinusoidal weighting function. A good sampling resolution (pixel size 6 mas) has been assumed in order to isolate the visibility effect. The simulated data visibility has been progressively reduced from 90% to 30%, introducing in the continuous PSF a nonmodulated component of the form

$$f(x) = \left(1 + \alpha + \cos\frac{2\pi}{T_Y}x\right)\exp\left(-\frac{x^2}{2\sigma^2}\right).$$

The same location process discussed above has been applied, using the optimal estimator w_p, 10^4 data samples, and fixed a priori phase. The results are shown in Figure 9, which illustrates the following results:

1. The location accuracy is close to the limiting value of ~0.20 mas (corresponding to 100% visibility) when the visibility is progressively reduced down to ~80%.
2. In the visibility range 80% down to 40%, the dispersion increases gradually up to 0.5 mas.
3. For visibility below 40%, the location accuracy decreases steeply toward the typical single aperture value (~1.4 mas): in this regime, the modulation information is basically lost, and the image profile approaches that of the single-aperture PSF.

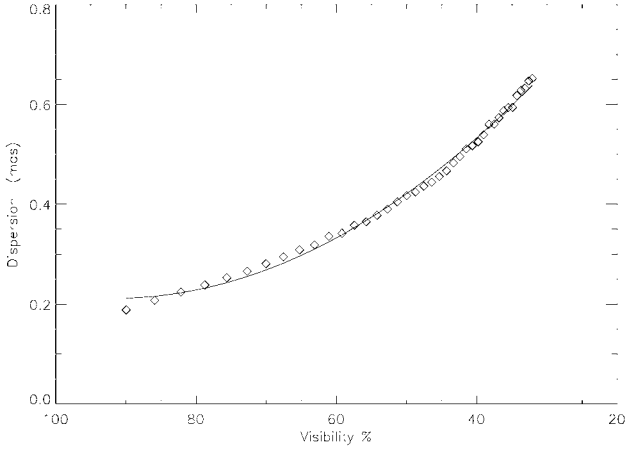

FIG. 9.— Simulated dispersion vs. visibility

The experimental points have been fitted to a polynomial function (Fig. 9), which provides a relation between visibility V_b and location dispersion σ:

$$\sigma(V_b) = 1.218\text{–}2.19 \times 10^{-2}V_b + 1.191 \times 10^{-4}V_b^2. \tag{25}$$

7. READ-OUT NOISE

Photon-limited analysis provides a useful preliminary assessment of the expected limiting performance, but a realistic study must at least account for the detector read-out noise.

The discussion so far suggests that increasing sampling resolution will improve the resulting location accuracy and, eventually, the astrometric accuracy, but that the limiting accuracy obtained from equation (1) is essentially achieved when ~10 pixels are placed in the fringe period, assuming negligible read-out noise (RON). However, each pixel provides its own RON contribution to the overall measured signal; therefore, it seems reasonable that, beyond a given resolution (i.e., below some pixel size), the increasing RON effects overcome the increasing geometric improvement.

The problem can be evaluated by means of the expressions from § 3 and can be simulated through the procedures described in § 5. Both approaches have been undertaken, with the results shown in Figures 10 and 11, respectively. A pixel size of 8 mas has been assumed, which corresponds to an intermediate, but still good, sampling resolution.

The general trend is similar for both estimated and simulated performance, since photon-limited accuracy at given geometry is obtained only in case of negligible RON: at increasing noise,

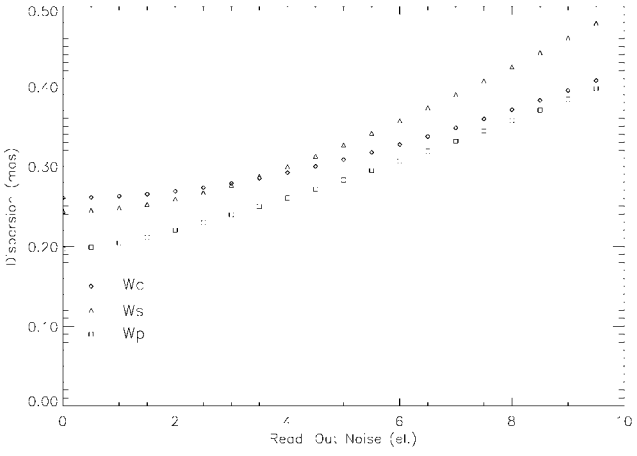

FIG. 10.— Estimated dispersion vs. read-out noise (pixel size= 8 mas)

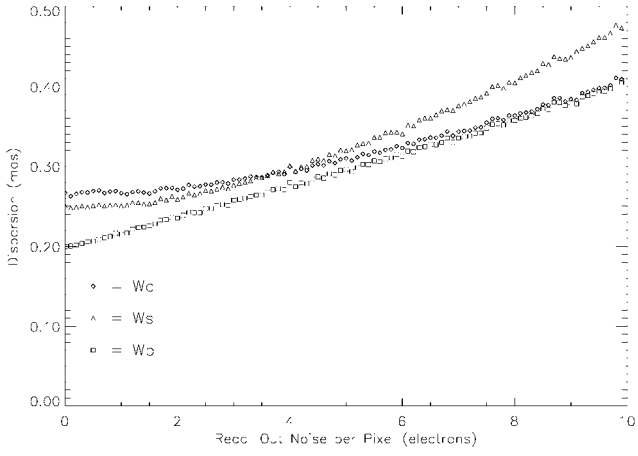

FIG. 11.— Simulated dispersion vs. read-out noise (pixel size= 8 mas)

the sinusoidal weighting function dispersion grows much faster than the other estimators, which merge for high read-out noise values. The latter aspect is consistent with the character of the correlation, which is the best estimator for the white-noise case.

For a realistic current RON value such 6 electrons pixel^{-1}, the dispersion increase is 50% with respect to the simulated data affected only by shot noise. Assuming a pixel size of 8 mas, the central part of the whole fringe pattern (i.e., the main Airy disk) is sampled over about 60 pixels; therefore, the *global* noise contribution is $\sqrt{60} = 7.7$ times larger than the single-pixel read-out noise value. This accounts for the significant degradation of the location accuracy even for relatively small RON: at 5 electrons pixel^{-1}, the overall noise variance is $5^2 \times 60 = 1500$, quite comparable with the intrinsic photon variance, owing to the Poisson statistics, of our reference signal (intensity 2000 photoelectrons), corresponding to a rather bright target ($V = 12.5$).

Scaling the accuracy for SNR only, accordingly to equation (1), the expected degradation is ~25%, from ~0.2 to ~0.26 mas. This is compatible with the estimated performance (Fig. 10) and slightly better than the value provided by the simulated data (Fig. 11). The consistency between the simulated and estimated dispersion values is reasonably good for rather bright targets, but a progressively increasing mismatch arises at increasing magnitude, i.e., with the reduction of the source photon flux. This should be expected, even taking into account some marginal gain obtained by algorithm optimization for the low S/N case. In fact, in this range, the location process provides estimates affected by large errors, of the order of several mas. Therefore the conditions of equation (12) are not satisfied (i.e., errors are not negligible with respect to the fringe semiperiod), and the series development can not be limited to the first-order terms providing some of our expressions.

The trend of location accuracy versus target star magnitude, for a single 0.2 s exposure, for given RON and sampling conditions, is shown in Figure 12. We recall that such instrumental magnitude depends on different system parameters: spectral bandwidth, integration time, collecting area, and several efficiency terms. Therefore, improvement of specific key parameters may well improve the overall performance curve, providing lower location dispersion over the whole magnitude range (e.g., increasing the photon budget) or at least reducing the performance degradation over the faint magnitude range (e.g., reducing the RON).

It can be noted that, with current parameters, the effects of RON are dominant for magnitudes higher than $V \simeq 16$. Therefore, the performance that can be expected for targets much fainter than $V = 15$ is rather poor, at least as far as the coherent FOV is concerned. The incoherent FOV, because of the much smaller RON contribution due to sampling over a reduced number of pixels, seems to be the best option for achieving intermediate location accuracy over faint targets, as stated in the original GAIA proposal.

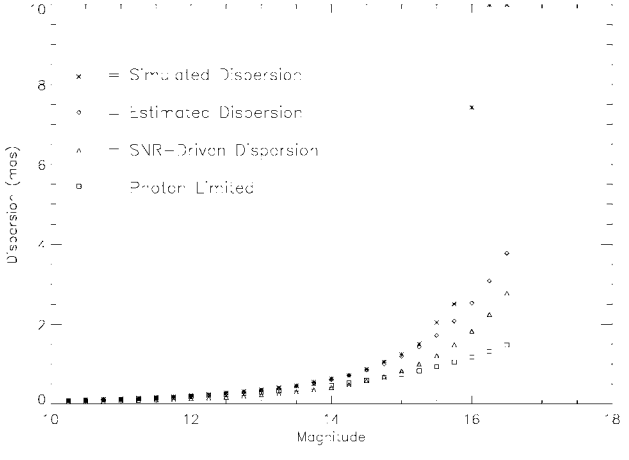

FIG. 12.— Estimated dispersion vs. magnitude (pixel size= 14 mas, RON = 3 e^-).

However, it is quite clear that, in order to achieve a reasonable location accuracy beyond the original survey limits, the RON must be as low as possible: values of the order of a few electrons are the best results currently achieved by the most advanced astronomical instrumentation.

The reduction of the RON contribution by reduction of the sampling resolution is in competition with the full exploitation of the intrinsic interferometer resolution: a trade-off on the sampling resolution is necessary, depending on the achievable RON level. For example, for our reference $V = 12.5$ mag target, at a RON $= 10\ e^-$ level, the optimal pixel size results to be 11.2 mas, and the location dispersion achieved is 0.4 mas; a $V = 15$ mag star is completely dominated by the RON, but in any case the optimal size is 14.9 mas; in the more favorable, but still realistic, case of RON $= 5\ e^-$, the optimal size is 12.2 mas, which provides a location dispersion of about 1.8 mas.

8. CONCLUSIONS

The effect of pixel finite size cannot be neglected for accurate target location from the focal plane images of the GAIA interferometers; however, in order to achieve the intrinsic limiting accuracy, impractical requirements arise for the spatial sampling resolution of the detection system. Dimensioning the detectors for sampling the fringe period over 4–5 pixels already provides about 27% degradation with respect to the asymptotic value, but increasing the resolution significantly (i.e., reducing the pixel size) will result in severe engineering problems because of the reduced geometry and extreme requirements on the read-out noise figure.

A progressive reduction of the resolution to little more than 2 pixels per fringe period degrades the location accuracy by about 50% with respect to the previous value, or about 80% with respect to the limiting (continuum) accuracy, using in any case the best algorithms currently available. The performance of the estimators is roughly comparable for realistic sampling resolution; in any case, the optimal weighting function is best, and correlation is worse, whereas the sine result is intermediate, when the RON is negligible; however, the former provides inconsistent results in some critical sampling resolution regions, which does not happen for the other estimators. Even in such cases, the bias effect can be removed by experimental calibration of the algorithm response; however, work is in progress to include appropriately the phase effects in the general mathematical description.

Including the effects of increasing RON, the sinusoidal weighting function performance degrades significantly, whereas the gap between the optimal weighting function and the correlation technique results is progressively reduced, which is consistent with general principles and the mathematical setup. If the RON and signal levels are fixed, an optimal pixel size can be identified; conversely, if the sampling resolution and RON are fixed, the location accuracy can be predicted fairly well over a wide target magnitude range. Since the limiting performance for faint targets is eventually dictated by the RON, it is important to improve the CCDs and/or to increase the elementary exposure time, which in the case of GAIA puts more stringent requirements on the optical configuration, the satellite attitude, or both.

Over a rather large range, the performance scales smoothly with the fringe visibility; therefore, coherence requirements do not seem to be exceedingly critical for the GAIA interferometers.

Given reasonable assumptions concerning the detectors available using current technology or those projected to be developed in the near-future, a fringe imaging detection system for GAIA seems to be feasible and able to provide quite interesting performance figures. Device optimization impacts directly on the survey limiting magnitude and astrometric performance.

The authors thank ESA for funding devoted to in-depth feasibility studies focused on GAIA and the colleagues involved therein for fruitful discussions on the overall system configuration and performance, which contributed to stimulate the analysis of the issues discussed in this paper.

Furthermore, our understanding of the problems benefited from discussions with members of the Scientific Advisory Group (appointed by ESA and currently working on the development of the GAIA mission concept) and with the ESA representatives managing the above studies.

This work was supported in part by NASA though grant NAGW-3861.

REFERENCES

Gai, M., et al. 1997a, in Proc. *Hipparcos*–Venice '97 Symposium (ESA SP-402), ed. B. Battrick (Noordwijk: ESA), 835
Gai, M., Guarnieri, M. D., & Lattanzi, M. G. 1997b, Exp. Astron., 7(2), 87
Gai, M., Lattanzi, M. G., Casertano, S., & Guarnieri, M. D. 1995, in Future Possibilities for Astronomy in Space (ESA SP-379), ed. M. A. C. Perryman & F. van Leeuwen (Noordwijk: ESA), 231
Lattanzi, M. G. 1995, in Future Possibilities for Astronomy in Space (ESA SP-379), ed. M. A. C. Perryman & F. van Leeuwen (Noordwijk: ESA), 301
Lattanzi, M. G., Gai, M., Cecconi, M., Cesare, S., & Mana, G. 1997, in Proc. 3d Internat. Conf. on Space Optics, ed. CNES (Toulouse), Session 2, Lecture 1
Lindegren, L. 1978, in IAU Colloq. 48, Modern Astrometry, ed. F. V. Prochazka & R. H. Tucker (Dordrecht: Reidel), 197
Lindegren, L., & Perryman, M. A. C. 1996, A&AS, 116, 579
Loiseau, S., & Shaklan, S. 1995, A&AS, 117, 167